

Ultra-Stable and Sensitive Ultraviolet Photodetectors Based on Monocrystalline Perovskite Thin Films

Xu Li, Chang Liu, Feng Ding, Zheyi Lu, Peng Gao, Ziwei Huang, Weiqi Dang, Liqiang Zhang, Xiaohui Lin, Shuimei Ding, Bailing Li, Ying Huangfu, Xiaohua Shen, Bo Li, Xuming Zou, Yuan Liu, Lei Liao, Yiliu Wang,* and Xidong Duan*

The detection of ultraviolet (UV) radiation with effective performance and robust stability is essential to practical applications. Metal halide single-crystal perovskites (ABX₃) are promising next-generation materials for UV detection. The device performance of all-inorganic CsPbCl₃ photodetectors (PDs) is still limited by inner imperfection of crystals grown in solution. Here wafer-scale single-crystal CsPbCl₃ thin films are successfully grown by vapor-phase epitaxy method, and the as-constructed PDs under UV light illumination exhibit an ultralow dark current of 7.18 pA, ultrahigh ON/OFF ratio of $\approx 5.22 \times 10^5$, competitive responsivity of 32.8 A W⁻¹, external quantum efficiency of 10867% and specific detectivity of 4.22×10^{12} Jones. More importantly, they feature superb long-term stability toward moisture and oxygen within twenty-one months, good temperature tolerances at low and high temperatures. The ability of the photodetector arrays for excellent UV light imaging is further demonstrated.

imaging for the diagnosis of high-tension transmission line, flame detection, ozone monitoring, astronomical observation, and short-wave communication,^[1–5] which raises high requirement on the related performances of UV-PDs, such as the large responsivity, high signal-to-noise ratio, fast response rate, high detectivity or sensitivity. However, though critical advances on mainstream UV-PDs have been achieved based on wide-bandgap inorganic semiconductors, including zinc oxide, gallium oxide, gallium nitride, Mg_xZn_{1-x}O, III-V compounds, which obtained superior performance to the silicon-based UV-PDs,^[6–10] the practical applications of PDs based on wide bandgap semiconductors have been severely limited by insufficient material performance, high-cost of man-

ufacturing, composition fluctuation, and phase separation during fabrication process, complicated device configurations, and relatively high operating voltage.^[11]

3D metal halide perovskites with an ABX₃ stoichiometry have shown great success in various optoelectronics, including solar cells, light-emitting diodes (LEDs), and radiation detectors.^[12–15] For UV detection, 3D all-inorganic metal halide perovskites with attractive properties (e.g., large light absorption coefficient, high carrier mobility, long carrier lifetime, low manufacturing cost, and high stability) have been considered as promising candidates for UV-PDs that to meet the aforementioned requirements.^[16–20] Among them, all-inorganic CsPbCl₃ with extraordinary ambient stability and temperature tolerance is especially appropriate for UV-PDs considering the matched wide bandgap (≈ 2.9 eV) that is selectively sensitive to UV signals.^[11,21–25] To further increase the performance of UV-PDs, single-crystal (SC) perovskites with fewer grain boundaries and lower trap densities, which possess superior properties, such as higher carrier mobility and longer carrier lifetime than the polycrystalline (PC) counterparts,^[26–28] have drawn extensive research interests.^[14,15,29–33] Generally, SC perovskite materials could be fabricated either by solution methods^[14,29,30,34–36] or vapor-phase epitaxy (VPE) methods.^[37–39] However, due to the poor solubility of the CsCl precursor in organic solvents, most solution-processed CsPbCl₃ grains are crystallized with small sizes (usually micro- or nanometers) and inevitably bring


1. Introduction

The development of ultraviolet (UV) detection has been falling behind the visible and infrared light detection due to the limitation of UV photodetector (PD). While the UV detection is of indispensable importance in variety of fields, including scientific research and practical applications, such as spectroscopy analysis for biochemical detection, corona

X. Li, C. Liu, Z. Lu, S. Ding, B. Li, X. Zou, Y. Liu, L. Liao, Y. Wang
School of Physics and Electronics
Hunan University
Changsha 410082, P. R. China
E-mail: yiliuwang@hnu.edu.cn

F. Ding, Z. Huang, W. Dang, L. Zhang, X. Lin, B. Li, Y. Huangfu,
X. Shen, X. Duan
College of Chemistry and Chemical Engineering
Hunan University
Changsha 410082, P. R. China
E-mail: xidongduan@hnu.edu.cn

P. Gao
Institute of Semiconductors
South China Normal University
Guangzhou 510631, P. R. China

 The ORCID identification number(s) for the author(s) of this article can be found under <https://doi.org/10.1002/adfm.202213360>.

DOI: 10.1002/adfm.202213360

about rough surficial morphologies of resultant PC films with numerous grain boundaries and a high density of defects,^[40–44] not only weakening the performance of as-constructed PDs but also limiting the application of large-scale UV image sensing. Besides, the thicknesses of the bulk single crystals grown by solution methods are usually uncontrollable, especially it's difficult to prepare quasi-2D morphology to make use of the well-developed integration technique,^[45–47] which curbs the demands for fabrications of thin-film (TF) perovskites-based devices. VPE growth technique has greater superiorities in morphology and grain size control and enables the monolithic integration.^[48–50] In 2017, Shi's group achieved centimeter-scale and grain boundary-free CsSnBr₃ and CsPbBr₃ SCTFs on alkali halide for the first time,^[37] whereafter, Jin's group produced CsPbBr₃ large-area (10 mm × 5 mm) SCTFs on SrTiO₃ substrate, by employing VPE method.^[38] Although, there are researchers who have used single-source vapor deposition (SSVD) method to deposit CsPbCl₃ films, the crystallinity of them is not monocrystalline.^[51,52] To date, to our knowledge, there have been rare reports about CsPbCl₃ SCTFs, hence, it is crucial to extend the VPE method to grow large-scale high-quality SCTFs of CsPbCl₃ for efficient and stable UV-PDs.

In this work, we have successfully grown wafer-scale phase-pure CsPbCl₃ SCTFs with excellent crystallinity and superior optoelectronic properties on muscovite via VPE. Meanwhile, we have fabricated lateral photoconductor-type PDs on as-grown CsPbCl₃ SCTFs by transferring Au electrodes without any charge separation layer or surface passivation layer. It is found that the present PDs under 375 nm laser illumination exhibit extraordinary device performance including an ultralow dark current of 7.18 pA, ultrahigh ON/OFF ratio of $\approx 5.22 \times 10^5$ at 279 W cm⁻² light illumination, competitive responsivity, external quantum efficiency, and specific detectivity of 32.8 A W⁻¹, 10867% and 4.22×10^{12} Jones at 4.4 μ W cm⁻² light illumination, respectively. More importantly, our UV-PDs exhibit overwhelming superiority in air ambiance stability at room temperature within twenty-one months, good high and low-temperature resistances and remarkable recoverability after the first consecutive fast rising–falling–rising temperature operation test.^[25,53] Furthermore, a CsPbCl₃ SCTF-based PD array for UV light image sensing is built and the photocurrent can maintain the initial value after three months.

2. Results and Discussion

2.1. Vapor Phase Deposition of CsPbCl₃ Thin Film

The CsPbCl₃ thin film has been deposited on the freshly exfoliated (001) surface of muscovite in a home-built chemical vapor deposition (CVD) system (the precursor was prepared by mixing CsCl and PbCl₂ with a molar ratio of 1:1, see Experimental Section and Figures S1–S5, Supporting Information for more details). The as-grown film under UV light displays a blue light emission over the entire substrate, while the spin-coated CsPbCl₃ TF does not show obvious blue emission under the same condition (Figure 1a). The blue light emission gives a direct visual indication of the high optical quality of the VPE-grown TF. Optical microscopy image shows a flat

and smooth surface without any grain boundaries or cracks (Figure 1b), which is further confirmed by scanning electron microscopy (SEM) image (Figure 1c), manifesting the high crystal quality of the CsPbCl₃ TF. 2D atom force microscopy (AFM) image shows that the as-grown CsPbCl₃ TF obtains a highly smooth surface with a root mean square roughness of ≈ 1.43 nm (Figure 1d), and no pinholes are observed. In the X-ray diffraction (XRD) spectra, the peaks from (00 l) planes of monoclinic muscovite have been marked with “*”, the other peaks are all assigned to the ($h00$) planes of the tetragonal phase CsPbCl₃ (JCPDS No. 18–0366; Figure 1e), suggesting a high out-of-plane orientation with the epitaxial relationship of CsPbCl₃ (100)||muscovite (001). The photoluminescence (PL) spectra collected from five random locations of the same TF, all five spectra, centered at about 414 nm which is consistent with the previously reported band-edge emission of CsPbCl₃, show similar symmetric shape and almost the same high intensities (Figure 1f), demonstrating the uniformity of CsPbCl₃ over the entire substrate. Energy dispersive X-ray spectroscopy (EDS) shows the atomic ratio of Cs, Pb, and Cl in the film is 20.0%:19.9%:60.2%, consistent to the stoichiometric ratio of 1:1:3 within the experimental error (Figure 1g), and the Cl composition highlights there are almost no existences of Cl vacancies (V_{Cl}) at the surface of the CsPbCl₃ TF compared to the previous report.^[54] The EDS elemental mapping further shows the homogeneous spatial distribution of all three elements (Figure 1g, inset). In order to probe the chemical composition and bond states of the three elements in the film, X-ray photoelectron spectroscopy (XPS) has been applied. The wide range XPS spectrum shows the signal peaks of Cs, Pb, and Cl were detected within a specific scan range (Figure S6, Supporting Information). The core-level XPS spectra of Cs, Pb, and Cl display that two peaks of Cs 3d_{3/2} and Cs 3d_{5/2} are located at 738.1 and 724.2 eV, respectively, two peaks of Pb 4f_{5/2} and Pb 4f_{7/2} are centered at 143.0 and 138.1 eV, respectively, and two peaks of Cl 2p_{1/2} and Cl 2p_{3/2} are located at 199.3 and 197.7 eV, respectively (Figure 1h). The energy deviation values of spin-orbit splitting in Cs 3d, Pb 4f, and Cl 2p are 13.9, 4.9, and 1.6 eV consistent with reported values^[55] and consistent to the ideal chemical bond configuration of CsPbCl₃. Furthermore, we postulated the crystal structure of the tetragonal perovskite CsPbCl₃ in Figure 1i, the corner-sharing PbCl₆⁴⁻ octahedrons stacked together with Cs⁺ cations occupying the interstitial site to stabilize the framework.

We conducted X-ray pole figure to verify the single-crystalline feature of CsPbCl₃ TF with centimeter scale on muscovite which has been shown in Figure 1a. The resulting pole figure measured at a fixed $2\theta = 22.43^\circ$ indexed to CsPbCl₃ (101) shows four symmetrical poles separated azimuthally by $\Phi = 90^\circ$ at a tilt angle of $\psi = 30^\circ$ corresponding to the four equivalent {101} family planes (Figure 2a), confirming the single-crystalline nature of the as-grown CsPbCl₃ TF with ordered in-plane orientation. The rocking curves for the (100) and (200) diffraction peaks have full width at half maximum (FWHM) of 0.18° and 0.15°, respectively (Figure 2b,c), consistent to the values of perovskite SCTF,^[38] supporting the single crystallinity of CsPbCl₃ TF has uniform out-of-plane orientation (Figure 1e). To estimate the thickness of the film, we cleaved the SiO₂/Si substrate with CsPbCl₃ film transferred on it to expose the

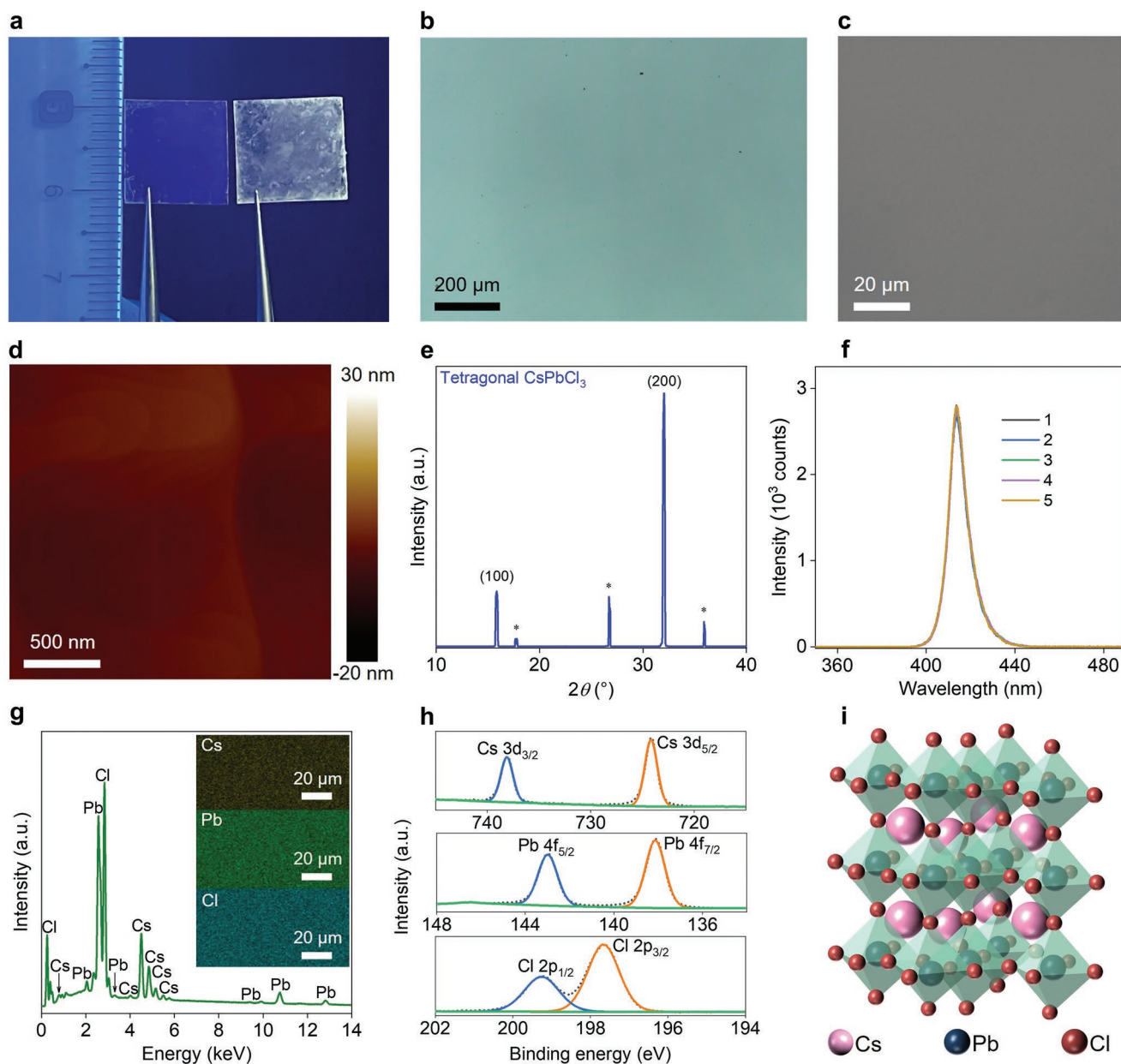


Figure 1. Structural characterizations of CsPbCl₃ TF grown on muscovite substrate. a) Photograph of the CsPbCl₃ TF (left) and spin-coated thin film (right) under UV light irradiation. Some non-uniformity located in edges seen in the photograph is attributed to accidental scratches when clamped with tweezers, rather than the intrinsic optical quality of the TF. b) Optical microscopy image of the CsPbCl₃ TF. c) Top-view SEM image of the CsPbCl₃ TF. d) AFM image of the surface topography of the CsPbCl₃ TF. e) XRD pattern of the CsPbCl₃ TF grown on muscovite substrate shows only (*h*00) planes. Peaks from (00*l*) planes of muscovite are marked with “*”. f) Five PL spectra randomly collected from different positions on one CsPbCl₃ TF. g) EDS analyses of the TF show the atomic ratios of Cs:Pb:Cl of 20.0%:19.9%:60.2%. The inset is the EDS elemental mapping, showing uniform dispersion of three compositional elements. h) XPS spectra corresponding to Cs 3d (top pane), Pb 4f (middle pane), and Cl 2p (bottom pane) of the CsPbCl₃ TF. i) Structural illustration of the tetragonal perovskite CsPbCl₃.

cross-section of the film. SEM image shows the thickness of CsPbCl₃ TF is about 1.86 μm, and there are not any grain boundaries and pinholes in large scale (Figure 2d and inset), indicating the high-quality of yielded CsPbCl₃ TF.

We used electron back-scattered diffraction (EBSD) to further confirm the large-area continuity and homogeneity of the obtained CsPbCl₃ TF. The EBSD phase distribution map shows the uniform color (Figure 2e), proving the pure phase

nature of the tetragonal CsPbCl₃ TF. The EBSD orientation maps along the x, y, and z axis present a single and continuous color, respectively (Figure 2f–h), confirming the single crystallographic orientation of CsPbCl₃ TF along the (100) direction. This uniform crystal orientation across the as-grown CsPbCl₃ TF on the centimeter scale is highly desirable for efficient charge transport in the perovskite-based optoelectronic devices.

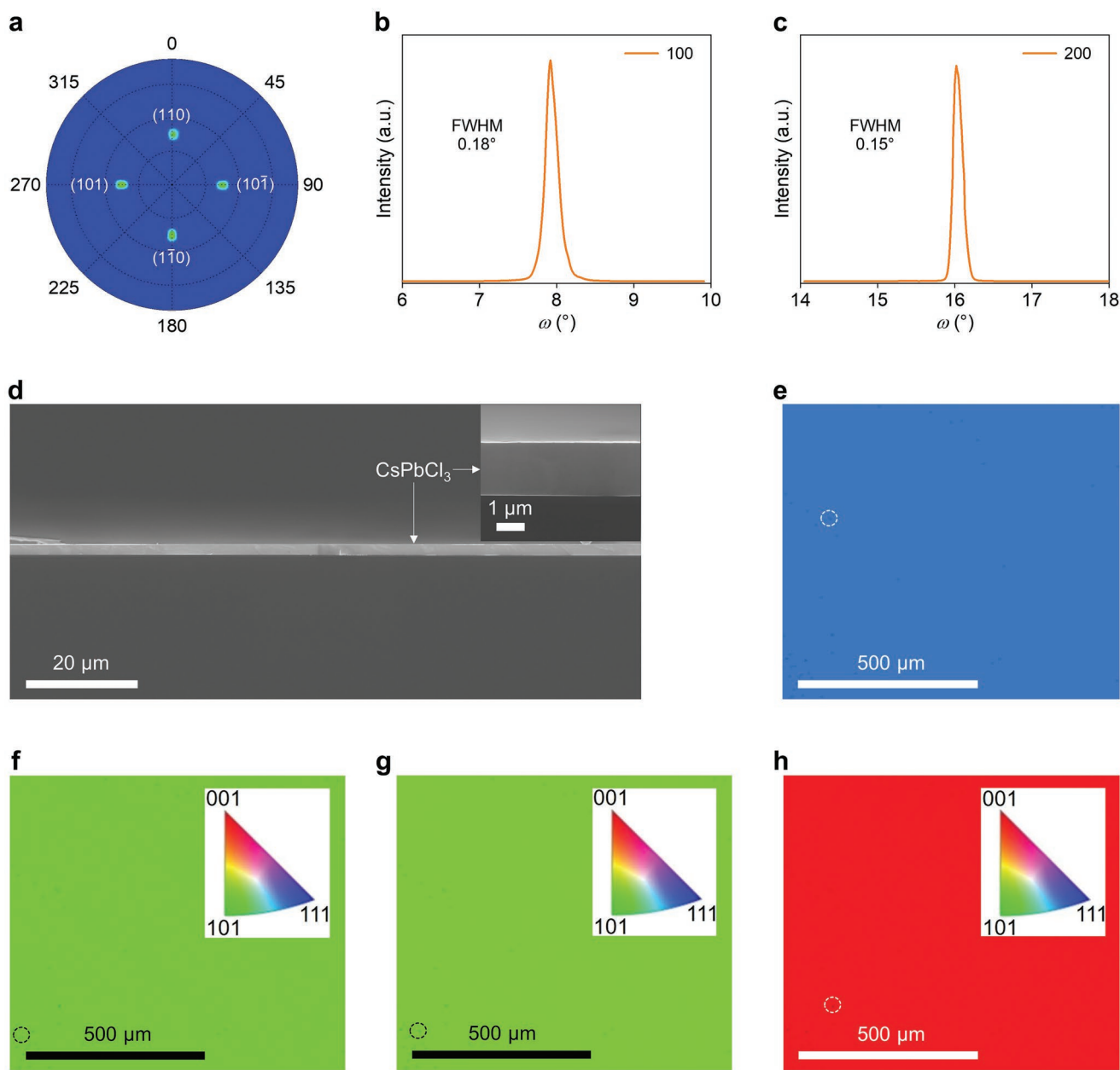


Figure 2. Crystalline characterizations of CsPbCl₃ TF. a) The {101} pole figure of the centimeter-scaled CsPbCl₃ TF showing four poles with equal intervals corresponding to symmetrical planes of the {101} family. b,c) XRD rocking curves of the CsPbCl₃ diffraction peaks at (100) and (200). d) Low magnification cross-section SEM image of the CsPbCl₃ TF transferred onto SiO₂/Si substrate. Inset is partial higher magnification cross-section SEM image of d). e) The phase distribution map of the CsPbCl₃ TF obtained from large-scale EBSD mapping. f–h) Inverse pole figures along the x-axis (IPF-X, f), y-axis (IPF-Y, g), and z-axis (IPF-Z, h) at the same region as that of phase map. Inset at the top right shows the color code map for IPF. Some unresolved phase counts ascribed to the dust adsorbing on the surface of TF are shown as a few of black dots, and some representatives of them are circled with dashed rings seen in (e–h).

2.2. Optical and Transport Properties of CsPbCl₃ SCTF

To evaluate the potential of our CsPbCl₃ SCTF for optoelectrical applications, we proceeded with the characterization of the absorption spectrum which shows a sharp absorption edge at ≈438 nm, and the PL peak is located at ≈414 nm with a FWHM of ≈9.6 nm, which matches well with the absorption

edge (Figure 3a; Figure S7, Supporting Information for more details). The Tauc plot calculated from the absorption spectrum displays an optical bandgap of 2.87 eV (Figure 3a, inset), in good agreement with the previous report.^[24] The work function (ϕ) of CsPbCl₃ SCTF was determined to be 5.84 eV with ultraviolet photoelectron spectroscopy (UPS, Figure 3b). The energy difference between the valence band maximum (E_{VBM}) and

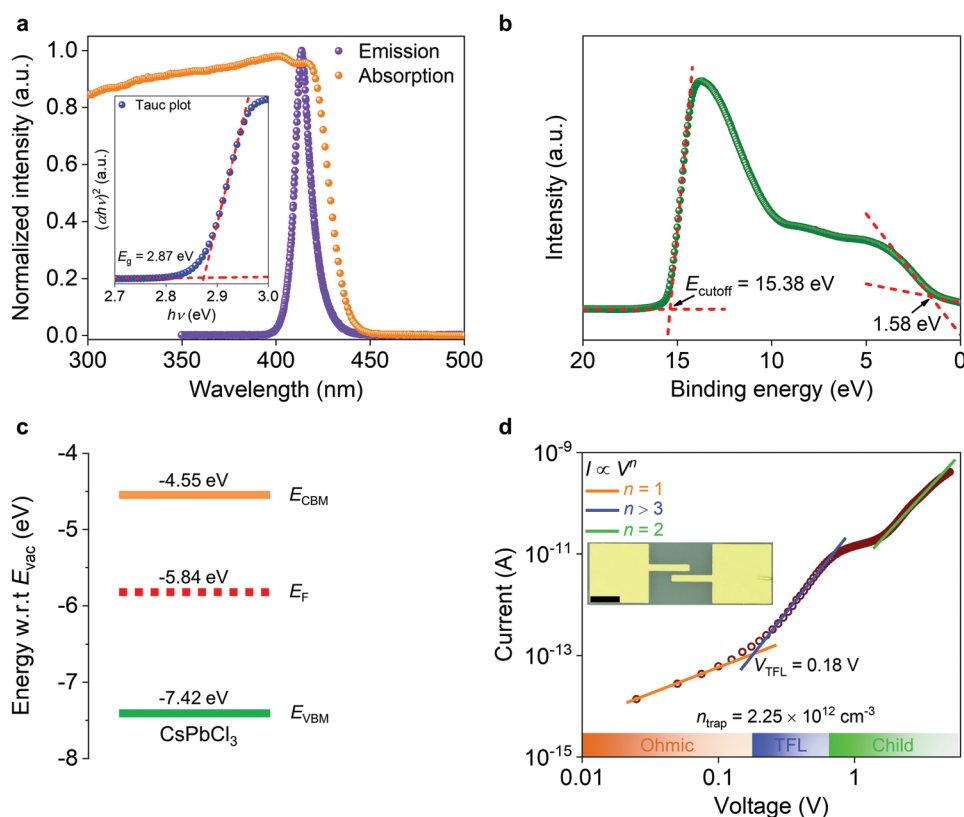


Figure 3. Optical and transport properties of CsPbCl₃ SCTF. a) UV-vis absorption spectrum of CsPbCl₃ powder and PL spectrum of CsPbCl₃ SCTF. The inset is calculation of the optical bandgap using the Tauc method assuming a direct bandgap. b) UPS spectrum of the CsPbCl₃ SCTF. c) Energy-level diagram of the CsPbCl₃ SCTF calculated from the Tauc plot and UPS result versus the vacuum level defined as 0 eV. d) Logarithmic *I*-*V* characteristic of the Au/CsPbCl₃ SCTF/Au device under dark condition showing three different regimes. The inset is the optical microscopy image of the device with lateral architecture. Scale bar: 50 μm.

Fermi energy level (E_F) is ≈ 1.58 eV read from the low-binding-energy region, with the corresponding VBM position being -742 eV. In combination with the bandgap (2.87 eV), the calculated conduction band minimum (E_{CBM}) of CsPbCl₃ SCTF is -4.55 eV. With the corresponding values above, the energy-level diagram of CsPbCl₃ SCTF is depicted in Figure 3c. We further estimated the trap density (n_{trap}) of the CsPbCl₃ SCTF using the space-charge-limited-current (SCLC) method,^[56,57] and a lateral gold (Au)/CsPbCl₃ SCTF/Au device with channel length and width of 30 and 6 μm, respectively, was fabricated by van der Waals (vdW) integration (Figure 3d, inset; see Experimental Section for more details).^[58] Three regions are identified in the logarithmic dark current-voltage (*I*-*V*) trace: the ohmic region (orange) at low voltages, the trap-filled limit (TFL) region (blue) at intermediate voltages, where all the available trap states are expected to be filled with the injected carriers, and the trap-free Child's regime (green) under high electric field (Figure 3d). The applied voltage at the kink point between the ohmic and TFL region is called TFL voltage (V_{TFL}) which is related to the n_{trap} .^[59]

$$V_{\text{TFL}} = \frac{en_{\text{trap}}d^2}{2\epsilon\epsilon_0} \quad (1)$$

where e is the elementary charge, d is the device channel width, ϵ is the relative dielectric constant of the CsPbCl₃ SCTF, and

ϵ_0 is the vacuum permittivity. In our device configuration, $d = 6$ μm, $\epsilon = 4.07$ for CsPbCl₃,^[60] and $V_{\text{TFL}} = 0.18$ V determined from Figure 3d. The calculated n_{trap} is 2.25×10^{12} cm⁻³, which is comparable to that of the CsPbCl₃ single crystals reported and several orders of magnitude lower than that of perovskite polycrystalline film.^[26,28,54,61-64]

With all the above superior properties including high uniformity and low trap density, we are inspired to develop the high-quality CsPbCl₃ SCTF into optoelectronic devices. Herein, lateral type PDs are designed and fabricated with photoconductor structure, i.e., a pair of Au electrodes are directly transferred onto the CsPbCl₃ SCTF and the effective illumination area (S) is 1.8×10^{-6} cm² (Figure S8a, Supporting Information; see Experimental Section for more details), which stay the same structure and channel size taken for SCLC method. Based on the energy-level diagram of the CsPbCl₃ SCTF, the energy-band alignment of the Au/CsPbCl₃ SCTF/Au configuration has been pictured for understanding the working mechanism of the device (Figure S8b, Supporting Information). Owing to the photoelectric effect, electron-hole pairs generated in CsPbCl₃ photoactive layer when the PD is irradiated via photons with energy larger than the bandgap of CsPbCl₃ (2.87 eV) will be separated and collected via the two electrodes under the external electric field, forming photocurrents.^[65]

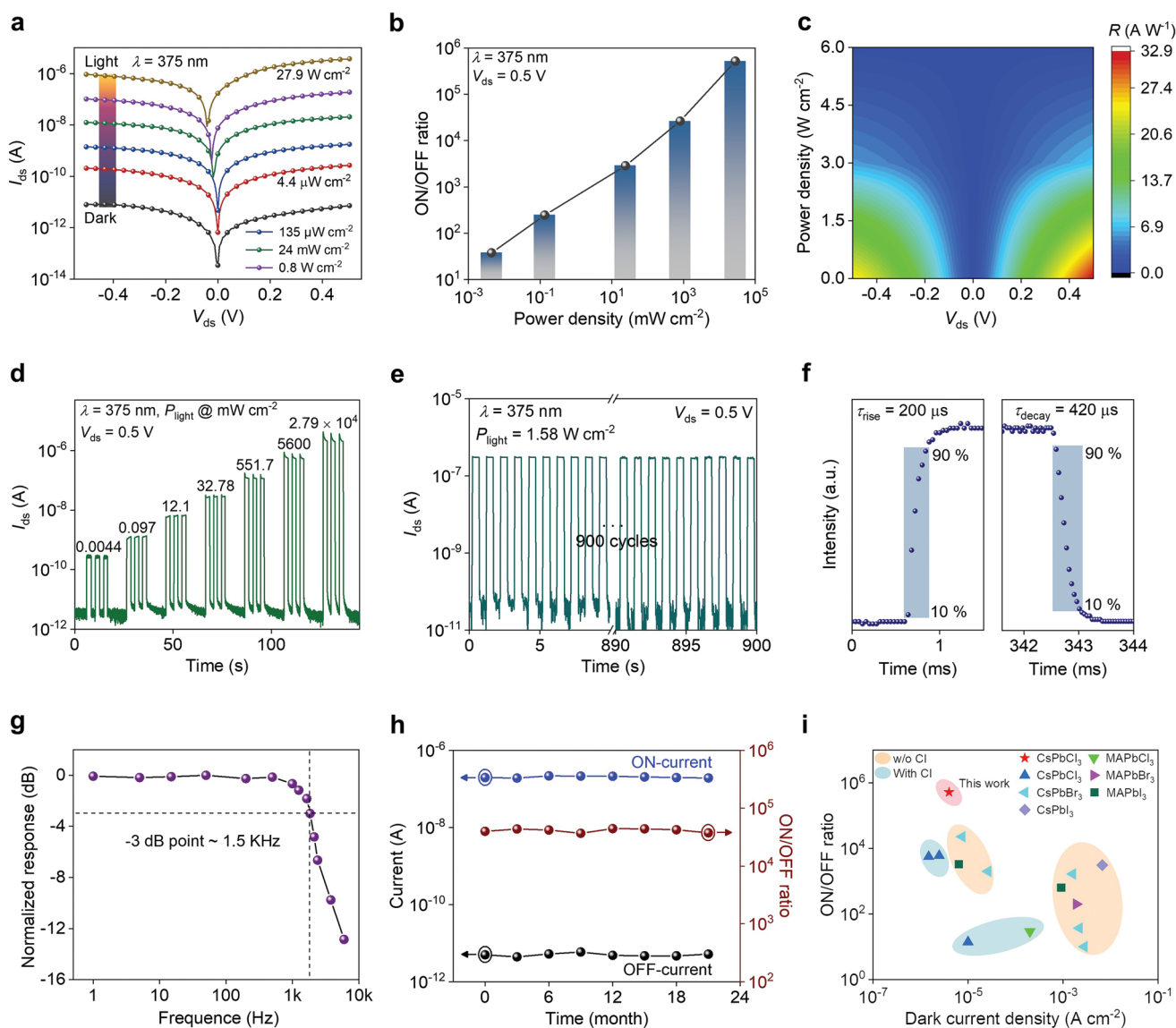


Figure 4. Performance of CsPbCl₃ SCTF-based PD. a) I_{ds} - V_{ds} curves of the device measured in dark and light. Here, the applied laser is 375 nm with P_{light} ranging from 4.4 $\mu\text{W cm}^{-2}$ to 27.9 W cm^{-2} . b) ON/OFF ratio values extracted from I_{ds} - V_{ds} curves in a) under a fixed 0.5 V bias. c) V_{ds} and P_{light} dependent responsivity extracted from I_{ds} - V_{ds} curves in a). d) I_{ds} - t photoresponse curves of the device recorded at $V_{ds} = 0.5$ V under 375 nm laser illumination at different P_{light} . e) Long-time switching stability of the device measured at $V_{ds} = 0.5$ V under 375 nm laser illumination at $P_{light} = 1.58$ W cm^{-2} . f) The tested response speed of the device under 375 nm laser illumination. g) Frequency-dependent response of the device. The dashed line shows the representative -3 dB bandwidth ($f_{-3\text{dB}}$) of ≈ 1.5 KHz. h) Plot of I_{dark} , I_{light} , and ON/OFF ratio values collected about every three months in twenty-one months measured at $V_{ds} = 0.5$ V under 375 nm laser illumination at $P_{light} = 922.5$ mW cm^{-2} . i) Comparison of dark current density and ON/OFF ratio among reported ABX₃-configurational perovskite material PDs. “w/o = without Cl” means the material not containing Cl element, “With Cl” means the material containing Cl element. References to the selected work can be found in Table S1 (Supporting Information).

2.3. Device Performance of CsPbCl₃ SCTF-Based PD

Figure 4a shows the I_{ds} - V_{ds} curves of CsPbCl₃ SCTF-based PD in the dark and light. To fully explore the performance of the device, here, we employed a 375 nm laser and performed a wide range of incident light power density (P_{light}) variations (from 4.4 $\mu\text{W cm}^{-2}$ to 27.9 W cm^{-2}). In dark, the dark current (I_{dark}) was measured to be only 718 pA at $V_{ds} = 0.5$ V which is among the top-ranking I_{dark} recorded from the reports (Table S1, Supporting Information). It is worth noting that the I_{dark} values

of the device vary from 1.59 to 718 pA with the bias voltages ranging from 0.1 to 0.5 V, in which the device presents an ultralow current level with a small amplitude of variation. This property can endow our device with an ultrahigh light-current (I_{light})-to-dark-current value (ON/OFF ratio) at an ultralow bias of 0.5 V (Figure 4b). It is obvious that even at a small power density of 4.4 $\mu\text{W cm}^{-2}$, the device still has an increased output current up to 268.4 pA, and the maximum I_{light} value can achieve 3.75 μA when P_{light} is increased to 27.9 W cm^{-2} , contributing to an ultrahigh ON/OFF ratio of $\approx 5.22 \times 10^5$. Such low

I_{dark} , high I_{light} , and high ON/OFF ratio demonstrate the effective response to the incident UV light achieved in our device, which is beneficial for increasing signal-to-noise ratio of PDs in practical applications for weak light detection.

Normally, three key figures-of-merit for PDs including responsivity (R), external quantum efficiency (EQE), and specific detectivity (D^*) are estimated to quantitatively evaluate their photodetection abilities. R determines how effectively the PD responds to the optical signal,^[66,67] which is defined by the equation:

$$R = \frac{I_{\text{light}} - I_{\text{dark}}}{P_{\text{light}}S} = \frac{I_{\text{ph}}}{P_{\text{light}}S} \quad (2)$$

where I_{ph} denotes the photocurrent. According to the $I_{\text{ds}}-V_{\text{ds}}$ curves, the responsivity is found to decrease as the P_{light} value increases, which is attributed to the increased recombination rate of photoexcited carriers under high light intensity. When $V_{\text{ds}} = 0.5$ V and $P_{\text{light}} = 4.4 \mu\text{W cm}^{-2}$, R reaches the maximum value of 32.8 A W^{-1} (Figure 4c), which is about 70 times higher than that of a solution-grown single CsPbCl_3 microplatelet PD, and also higher than most of photoactive material UV-PDs reported (Table S2, Supporting Information). Meanwhile, EQE represents the photoelectron conversion efficiency defined as:^[68]

$$EQE = R \frac{hc}{\lambda e} \quad (3)$$

where R represents the responsivity, h is the Planck constant, λ is the wavelength of incident light, and c is the velocity of light. Here, EQE is obtained as high as 10867% simultaneously (Figure S9, Supporting Information), which is of more competitive strength compared to the reported photoactive material UV-PDs (Table S2, Supporting Information). Figure 4d depicts the $I_{\text{ds}}-t$ photoreponse curves of the device recorded at $V_{\text{ds}} = 0.5$ V under 375 nm laser illumination with changed P_{light} . It is obvious that the device can be switched on and off repeatedly and stably at various P_{light} from weak to strong. Furthermore, long-term ON/OFF switching test of the device was performed at $V_{\text{ds}} = 0.5$ V under 375 nm laser illumination (Figure 4e), the repeatable and prompt photocurrent response could be maintained in 900 cycles at $P_{\text{light}} = 1.58 \text{ W cm}^{-2}$, proving an outstanding cycling stability of the device. The response speed of PD is critical for catching rapid varying optical signal. As shown in Figure 4f, the rise time (τ_{rise}) and decay time (τ_{decay}) were estimated to be 200 and 420 μs , respectively, by a digital oscilloscope. Here, the τ_{decay} shows a slower decay rate which could be attributed to the presence of surface states trapping photocarriers from immediate collection or recombination after switching off illumination.^[69] Figure 4g depicts the plot of the frequency responses of the device, showing a -3 dB cutoff frequency up to ≈ 1.5 KHz. The fast photocurrent response of our device could be attributed to the very low trap density of the SCTF, which decreases the trapping effect on photogenerated carriers.

To evaluate the environmental stability of the device, we just kept the as-fabricated device without encapsulation in air at room temperature, and collected $I_{\text{ds}}-V_{\text{ds}}$ curves measured in dark and under 375 nm laser illumination at $P_{\text{light}} =$

922.5 mW cm^{-2} about every three months for twenty-one-month time period (Figure S10, Supporting Information). The plot of I_{dark} , I_{light} , and ON/OFF ratio values measured at $V_{\text{ds}} = 0.5$ V extracted from $I_{\text{ds}}-V_{\text{ds}}$ curves in Figure S10 (Supporting Information) shows three traces with tiny fluctuations, respectively (Figure 4h), demonstrating the high stability of our devices toward moisture and oxygen. In addition, no crystal structure changes were detected in the XRD survey spectra after seventeen months of storage in the same ambient conditions (Figure S11, Supporting Information). This merit is beneficial for practical applications of the CsPbCl_3 UV-PDs. Figure 4i shows a comparison of dark current density and ON/OFF ratio among other reported perovskite with an ABX_3 stoichiometry material PDs. Our CsPbCl_3 SCTF-based PD (in red) exhibits an ultralow dark current density and an ultrahigh ON/OFF ratio compared with that based on 3D perovskite materials in photoconductor mode.

Next, we evaluate the specific detectivity (D^*), which characterizes the capability of the device upon detecting weak optical signals.^[66,70] The D^* value can be estimated by the following relationship:

$$D^* = \frac{(SB)^{1/2}}{NEP} \quad (4)$$

$$NEP = \frac{(\overline{i_n^2})^{1/2}}{R} \quad (5)$$

where B denotes the bandwidth, NEP refers to the noise equivalent power, and $(\overline{i_n^2})^{1/2}$ represents the root-mean-square (RMS) value of the noise current. In detail, Figure 5a exhibits the dark noise spectral density measured at different V_{ds} ranging from 0.1 to 0.5 V. It should be noted that the densities undergo a minor change along with applied V_{ds} , which matches well with the variation trend of I_{dark} manifested in the $I_{\text{ds}}-V_{\text{ds}}$ curves (Figure 4a). Here, the noise level per unit bandwidth (1 Hz) of the device is extracted to be $1.04 \times 10^{-14} \text{ A Hz}^{-1/2}$ at $V_{\text{ds}} = 0.5$ V (Figure 5a). Using the maximum R value of 32.8 A W^{-1} , the minimum NEP is obtained to be $3.18 \times 10^{-16} \text{ W Hz}^{-1/2}$ (Figure S12, Supporting Information), and D^* reaches its maximum value of $4.22 \times 10^{12} \text{ cm Hz}^{1/2} \text{ W}^{-1}$ (Jones, Figure 5b), which is comparable to the reported best individual photoactive material UV-PDs (Table S2, Supporting Information). Comparing the performance of photoactive material PDs reported in this work to the state-of-the-arts, the parameters of ON/OFF ratio (Table S1, Supporting Information) and R , EQE , D^* (Table S2, Supporting Information) evidently demonstrate the superior performance achieved in our devices, which is attributed to the high crystal quality of CsPbCl_3 SCTF, the strong light-matter interaction, and the enhancement of carrier transport between metal-semi contacts beneficial from vdW contact.^[58,71] We also measured R and EQE values of this device under other lasers illumination with longer wavelengths, and R reach their values of 0.21 (referring to 375 nm laser), 9.39×10^{-4} , 6.46×10^{-4} , and $4.3 \times 10^{-5} \text{ A W}^{-1}$, and EQE values are obtained to be 70% (referring to 375 nm laser), 0.26%, 0.15% and 0.0081% at $V_{\text{ds}} = 0.5$ V and $P_{\text{light}} = 100 \text{ mW cm}^{-2}$ under 450, 532, and 660 nm lasers illumination, respectively (Figure S13, Supporting Information). It is

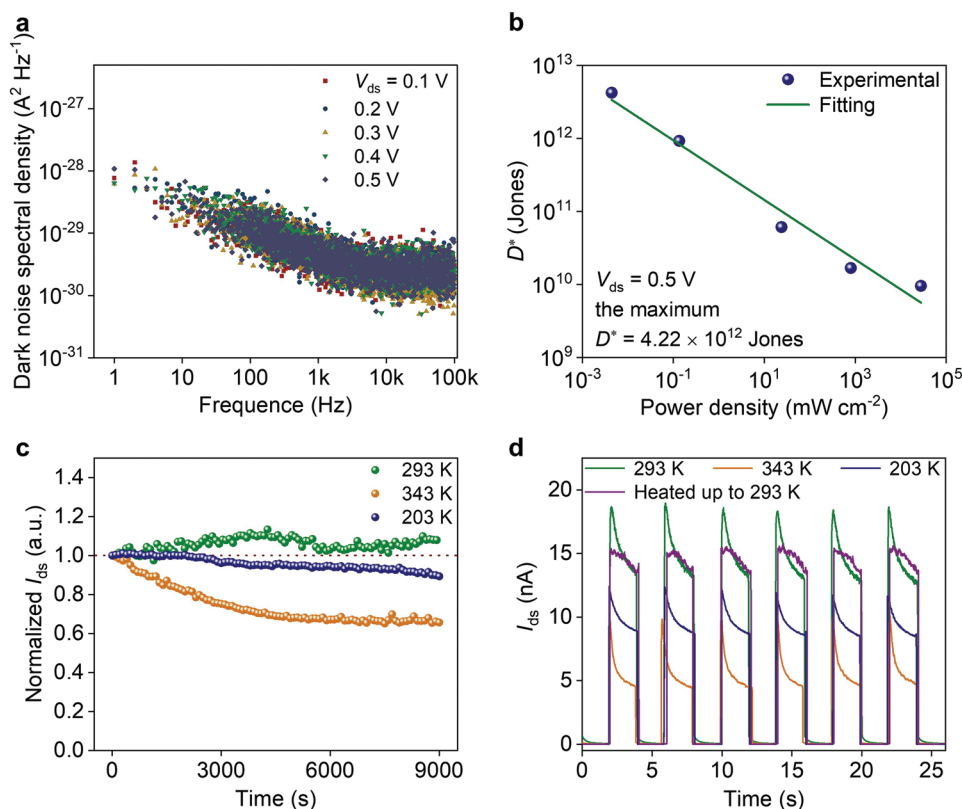


Figure 5. Performance of CsPbCl₃ SCTF-based PD. a) Dark noise spectral density measured at different V_{ds} . b) The extracted D^* at $V_{ds} = 0.5$ V. c) Normalized I_{ds} of the CsPbCl₃ SCTF-based PD versus running time at changed temperature in the order from 293 to 343 K and then to 203 K. d) Temporal photoresponse curves of the device at 293, 343, 203 K and after heated up to 293 K. All of the temperature-changing processes were manipulated in about 20 min.

obvious that both R and EQE values decrease with incident laser wavelength increasing (extending to the range of visible light) and suffer severe declines, where, for example, R and EQE values decrease by a factor of 223 and 269 times, respectively, when λ increases from 375 to 450 nm. These decreases are consistent with the optical bandgap of CsPbCl₃. According to our absorption test (Figure 3a and inset), the optical bandgap of CsPbCl₃ is 2.87 eV, i.e., 433 nm, and the lights with wavelengths longer than 433 nm are not going to be absorbed, so, photogenerated carriers are not going to be generated in CsPbCl₃ photoactive layer when this device is irradiated by these lights. Therefore, our device has the advantage in UV light selective response.

It is well-known that the long-term operation stability shown in harsh environment is a challenge for perovskite-based optoelectronic devices, considering the demand for operation with inconsistent conditions in actual application. To further prove the as-proposed stability of our device, the aging test was performed at a changed temperature in the order from 293 to 343 K and then to 203 K, and the normalized I_{ds} versus running time at $V_{ds} = 0.5$ V and $P_{light} = 21.4$ mW cm⁻² under 375 nm laser continuing illumination is shown in Figure 5c. It is obvious that I_{ds} of our PD exhibits a stable behavior after operation continuously for 2.5 h without any loss with respect to the original I_{ds} at 293 K, confirming the device possesses an excellent operation stability at room temperature. For assessing the temperature tolerance of our device, we next elevated the tem-

perature to 343 K, and I_{ds} drops rapidly and eventually maintains at a steady level of $\approx 65\%$. This phenomenon of the reduction of I_{ds} could be attributed to the phase transition occurring on the CsPbCl₃ SCTF at high temperature, which leads to the elevation of the Schottky barrier and consequently decreases the carrier transport efficiency. Intriguingly, when the working temperature fell to 203 K, I_{ds} just suffers a degraded decrease to $\approx 89\%$ of the initial value after continuous working for 2.5 h. This less decline in I_{ds} could be attributed to the enhanced effect of Schottky barrier on the device at low temperature compared to that at room temperature during working hours. We also tested the temporal photoresponse curves of the device in the process of one-time fast heating, cooling, and heating under the same conditions. As shown in Figure 5d, I_{ds} value at 203 K is bigger than that at 343 K, demonstrating better operation stability at low temperature than that at high temperature, and our PD could also achieve fast photoresponse at varied temperatures. An additional and very important observation is that after heated up to 293 K, I_{ds} could recover to 92% of the original level, which indicates a recoverable behavior of I_{ds} of our device after undergoing a fast process of rising–falling–rising temperature. The above tests prove the stable and recoverable performance of as-fabricated CsPbCl₃ SCTF-based PD even operated at high and low temperatures and also demonstrate the suitable compatibility of our device for practical applications under changed harsh conditions.

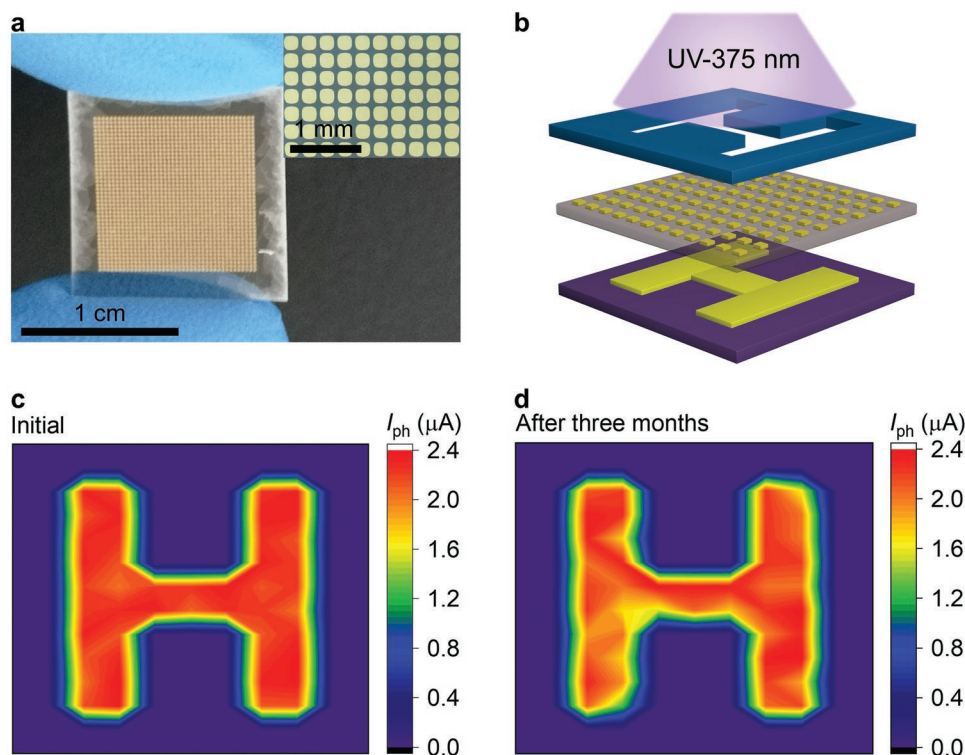


Figure 6. Image sensor based on the CsPbCl₃ SCTF. a) Photograph of electrode arrays on the CsPbCl₃ SCTF. Inset shows the partial corresponding optical microscopy image. b) Schematic illustration of a CsPbCl₃ SCTF-based PD array for UV light image sensing. c) Photocurrent mapping of the PD arrays with the H-shaped mask. d) Photocurrent mapping of the PD arrays with the H-shaped mask after three months of ambient exposure.

2.4. Image Sensor Based on the CsPbCl₃ SCTF

To demonstrate large-area integration, PD arrays for real-time UV light trajectories and multipoint light distribution is constructed (Figure 6a). As shown in Figure 6b, the pixels generate the photocurrent for the letter pattern area under UV light illumination while the other pixels produce the dark current for the region blocked by the designed mask. According to the mapping result, a clear “H” letter can be identified (Figure 6c), which demonstrates the ability to realize imaging function of fabricated PD arrays. Here, the long-term stability of the PD arrays is also evaluated upon ambient exposure for three months. As shown in Figure 6d, the resulting photocurrent is obtained without any loss, furtherly manifesting the excellent long-term stability of our CsPbCl₃ SCTF-based PD.

Here, we give some explanations for the superb stability: its intrinsic better environmental and high-temperature stability compared with organic-inorganic hybrid one due to its all-inorganic composition without any organic cations; its desirable tolerance factor of 0.87 closer to 1 compared to that of CsPbBr₃ (0.81) and CsPbI₃ (0.80);^[72–74] no V_{Cl} sites on the surface of it, which can suppress ion migration and subsequently improve electronic stability of it;^[75–78] no chemical bonding between the capping ligands and the inorganic surface due to the solvent-free growth surroundings, leading to reduced dynamic chemical instability compared with solution-processed one;^[79–81] and the single-crystalline nature acquired by VPE method granting immunization from grain boundaries and defects, which are the origins of degradation of perovskites.

3. Conclusion

In summary, we have demonstrated that wafer-scale phase-pure CsPbCl₃ single-crystal thin films can be grown on muscovite (001) substrates by employing vapor-phase epitaxy method for the first time. The resulting CsPbCl₃ SCTFs exhibit excellent crystal quality and superior optoelectrical properties, such as low trap density, comparable to those of CsPbCl₃ bulk crystals. We further fabricated UV photodetectors based on the high-quality monocrystalline thin film. An ultralow dark current of 7.18 pA has been obtained in the UV-PDs, and the high photoresponse enabled competitive responsivity of 32.8 A W⁻¹ and external quantum efficiency of 10867%, which resulted in excellent ON/OFF ratio of $\approx 5.22 \times 10^5$, and specific detectivity of 4.22×10^{12} Jones. More importantly, our devices show overwhelming superiority in long-term stabilities including the stability toward moisture and oxygen within twenty-one months. There is no current decay after continuous operation for 2.5 h at $P_{\text{light}} = 21.4 \text{ mW cm}^{-2}$ at room temperature, and remarkable recoverability has been achieved with $\approx 92\%$ of the initial current after a consecutive fast rising-falling-rising temperature operation test. In order to demonstrate the ability to realize practical application, we fabricated the CsPbCl₃ SCTF-based PD arrays in large scale, exhibiting excellent UV light imaging and high stability within three months. The unique optoelectrical properties and extraordinary stabilities make the as-obtained CsPbCl₃ SCTF may become a promising candidate for UV detection and imaging.

4. Experimental Section

Materials Growth: In this work, CsCl and PbCl₂ powders were mixed well with a molar ratio of 1:1 followed by solid-state reaction. Then, the mixture was heated to 400 °C and the temperature was maintained for 12 h to ensure a complete reaction to obtain CsPbCl₃ powder. Subsequently, the CsPbCl₃ powder source was placed at the center of the home-built CVD system, and the freshly exfoliated muscovite was placed at the downstream. The system was pumped down to base pressure and flushed with argon gas three times before, then, the pressure was stabilized at 50 mbar with Ar flow at a rate of 100 sccm as the carrier gas. The heating temperature was kept at 650 °C for 30 min for the completion of CsPbCl₃ film epitaxy with a thickness of 1.86 μm.

Materials Characterization: The optical images were taken with an optical microscope (Olympus DP27), the SEM morphology images, EDS and EBSD measurements were taken with a scanning electron microscope (TESCAN MIRA4 LMH) equipped with energy dispersive X-ray spectrometer (One Max 50) and electron back-scattered diffraction detector (Oxford Instruments NordlysMax3), the AFM image was performed with an atomic force microscope (BRUCKER Bioscope system), the XRD pattern and pole figure were collected using an X-ray diffractometer (Rigaku SmartLab SE) with the Cu Kα radiation, the XRD rocking curves were measured using a diffractometer (Panalytical X'Pert³ MRD) with Ge (220) hybrid monochromator incident beam optics, PL spectra were collected using a confocal microscope (Renishaw inVia Reflex) with a 355 nm laser as the excitation source, the XPS data was measured using a photoelectron spectrometer (Shimadzu AXIS SUPRA+), the absorption spectra were collected using a UV–vis–NIR spectrophotometer (Shimadzu UV-3600Plus) equipped with an integrating sphere attachment and the UPS data was measured using a photoelectron spectrometer (Thermo Fisher Scientific ESCALAB 250Xi).

Device Fabrication: For the device for SCLC measurements, 50 nm-thick Au metal electrodes were first deposited on a sacrificial SiO₂/Si substrate through the standard photolithography or electron-beam lithography followed high-vacuum (5×10^{-4} Pa) thermal evaporation process. Then, the whole wafer with Au electrodes was immersed in a sealed hexamethyldisilazane (HMDS) chamber to functionalize the surface of SiO₂ at 85 °C for 40 min. Next, polymethyl methacrylate (PMMA) was spin-coated on top of the Au electrodes to pick them up. Finally, the PMMA layer with 50 nm-thick Au electrodes within it was peeled off by polydimethylsiloxane (PDMS) stamp and laminated to the CsPbCl₃ thin film via the transfer platform under an optical microscope, the substrate was heated to 120 °C for 5 min to release the PMMA layer. The photodetectors were fabricated with the same technique. After the completion of Au electrodes transferred onto the CsPbCl₃ thin film, the device was first immersed in fresh trichloromethane (TCM) for 5 min to dissolve PMMA layer. Then, the device was washed with isopropanol (IPA) for several seconds and blow-dried. For the device for image sensing, 50 nm-thick square-liked Au metal electrode arrays were first thermally evaporated through a shadow mask on a sacrificial SiO₂/Si substrate. The transfer procedures were the same as that of aforementioned devices. But the PMMA layer with 50 nm-thick Au electrode arrays was mechanically peeled by thermal release tape and laminated directly to the CsPbCl₃ thin film and heated to 120 °C for 5 min to release the PMMA layer. The PMMA was also removed with TCM as aforementioned.

Device Characterization: Electrical and photoelectrical measurements were carried out on a probe station (Lakeshore TTP4) equipped with a semiconductor parameter analyzer (Agilent B1500A) under vacuum condition ($\approx 1.5 \times 10^{-4}$ Pa). Lasers with different wavelengths of 375, 450, 532, and 660 nm, respectively, were utilized as the illumination sources.

Supporting Information

Supporting Information is available from the Wiley Online Library or from the author.

Acknowledgements

The authors acknowledge financial support from the National Natural Science Foundation of China (grant nos. 62204081, and 51872086), and the Innovative Research Groups of Hunan Province (grant no. 2020JJ1001).

Conflict of Interest

The authors declare no conflict of interest.

Author Contributions

X.L., C.L., and F.D. contributed equally to this work. Y.W. and X.D. conceived the research and designed the experiments. X.L. and F.D. performed the film growth. X.L., F.D., Z.H., W.D., L.Z., X.L., B.L., Y.H., and X.S. performed material characterizations. X.L., C.L., Z.L., and S.D. fabricated the device. X.L. and C.L. measured the device. X.D., Y.W., L.L., Y.L., X.Z., B.L., C.L., and P.G. contributed to discussions. X.L., Y.W., and X.D. wrote the manuscript. All authors discussed the results and commented on the manuscript.

Data Availability Statement

The data that support the findings of this study are available from the corresponding author upon reasonable request.

Keywords

all-inorganic metal halide perovskites, monocrystalline CsPbCl₃ thin films, ultraviolet imaging sensing, ultraviolet photodetectors, vapor-phase epitaxy

Received: November 17, 2022

Revised: December 26, 2022

Published online: January 20, 2023

- [1] X. Wang, W. Tian, M. Liao, Y. Bando, D. Golberg, *Chem. Soc. Rev.* **2014**, *43*, 1400.
- [2] G. Konstantatos, E. H. Sargent, *Nat. Nanotechnol.* **2010**, *5*, 391.
- [3] P. Cheong, K.-F. Chang, Y.-H. Lai, S.-K. Ho, I.-K. Sou, K.-W. Tam, *IEEE Trans. Ind. Electron.* **2011**, *58*, 5271.
- [4] W. Zhou, H. Li, X. Yi, J. Tu, J. Yu, *IEEE Trans. Dielect. Elect. Insul.* **2011**, *18*, 232.
- [5] H. Chen, K. Liu, L. Hu, A. A. Al-Ghamdi, X. Fang, *Mater. Today* **2015**, *18*, 493.
- [6] W. Tian, C. Zhang, T. Zhai, S.-L. Li, X. Wang, J. Liu, X. Jie, D. Liu, M. Liao, Y. Koide, D. Golberg, Y. Bando, *Adv. Mater.* **2014**, *26*, 3088.
- [7] M. Reddeppa, N. T. KimPhung, G. Murali, K. S. Pasupuleti, B.-G. Park, I. In, M.-D. Kim, *Sens. Actuators B: Chem.* **2021**, *329*, 129175.
- [8] C. Xie, X.-T. Lu, X.-W. Tong, Z.-X. Zhang, F.-X. Liang, L. Liang, L.-B. Luo, Y.-C. Wu, *Adv. Funct. Mater.* **2019**, *29*, 1806006.
- [9] T. Lin, X. Liu, B. Zhou, Z. Zhan, A. N. Cartwright, M. T. Swihart, *Adv. Funct. Mater.* **2014**, *24*, 6016.
- [10] Z. Xia, K. Zang, D. Liu, M. Zhou, T.-J. Kim, H. Zhang, M. Xue, J. Park, M. Morea, J. H. Ryu, T.-H. Chang, J. Kim, S. Gong, T. I. Kamins, Z. Yu, Z. Wang, J. S. Harris, Z. Ma, *Appl. Phys. Lett.* **2017**, *111*, 081109.

- [11] L. Sang, M. Liao, M. Sumiya, *Sensors* **2013**, *13*, 10482.
- [12] R. Azmi, E. Ugur, A. Seitkhan, F. Aljamaan, A. S. Subbiah, J. Liu, G. T. Harrison, M. I. Nugraha, M. K. Eswaran, M. Babics, Y. Chen, F. Xu, T. G. Allen, A. U. Rehman, C.-L. Wang, T. D. Anthopoulos, U. Schwingenschlögl, M. De Bastiani, E. Aydin, S. De Wolf, *Science* **2022**, *376*, 73.
- [13] K. Lin, J. Xing, L. N. Quan, F. P. G. de Arquer, X. Gong, J. Lu, L. Xie, W. Zhao, D. Zhang, C. Yan, W. Li, X. Liu, Y. Lu, J. Kirman, E. H. Sargent, Q. Xiong, Z. Wei, *Nature* **2018**, *562*, 245.
- [14] J. Jiang, M. Xiong, K. Fan, C. Bao, D. Xin, Z. Pan, L. Fei, H. Huang, L. Zhou, K. Yao, X. Zheng, L. Shen, F. Gao, *Nat. Photonics* **2022**, *16*, 575.
- [15] Y. He, M. Petryk, Z. Liu, D. G. Chica, I. Hadar, C. Leak, W. Ke, I. Spanopoulos, W. Lin, D. Y. Chung, B. W. Wessels, Z. He, M. G. Kanatzidis, *Nat. Photonics* **2021**, *15*, 36.
- [16] Z. Guo, Y. Wan, M. Yang, J. Snaider, K. Zhu, L. Huang, *Science* **2017**, *356*, 59.
- [17] D. W. de Quillettes, S. M. Vorpahl, S. D. Stranks, H. Nagaoka, G. E. Eperon, M. E. Ziffer, H. J. Snaith, D. S. Ginger, *Science* **2015**, *348*, 683.
- [18] G. Xing, N. Mathews, S. Sun, S. S. Lim, Y. M. Lam, M. Grätzel, S. Mhaisalkar, T. C. Sum, *Science* **2013**, *342*, 344.
- [19] M. Zhang, M. Lyu, H. Yu, J.-H. Yun, Q. Wang, L. Wang, *Chem. - Eur. J.* **2015**, *21*, 434.
- [20] W. Hui, L. Chao, H. Lu, F. Xia, Q. Wei, Z. Su, T. Niu, L. Tao, B. Du, D. Li, Y. Wang, H. Dong, S. Zuo, B. Li, W. Shi, X. Ran, P. Li, H. Zhang, Z. Wu, C. Ran, L. Song, G. Xing, X. Gao, J. Zhang, Y. Xia, Y. Chen, W. Huang, *Science* **2021**, *371*, 1359.
- [21] M. Gong, R. Sakidja, R. Goul, D. Ewing, M. Casper, A. Stramel, A. Elliot, J. Z. Wu, *ACS Nano* **2019**, *13*, 3714.
- [22] C. Luo, C. Yan, W. Li, F. Chun, M. Xie, Z. Zhu, Y. Gao, B. Guo, W. Yang, *Adv. Funct. Mater.* **2020**, *30*, 2000026.
- [23] W. Li, J. Li, G. Niu, L. Wang, *J. Mater. Chem. A* **2016**, *4*, 11688.
- [24] L. Protesescu, S. Yakunin, M. I. Bodnarchuk, F. Krieg, R. Caputo, C. H. Hendon, R. X. Yang, A. Walsh, M. V. Kovalenko, *Nano Lett.* **2015**, *15*, 3692.
- [25] Y. Li, Z. Shi, L. Lei, Z. Ma, F. Zhang, S. Li, D. Wu, T. Xu, X. Li, C. Shan, G. Du, *ACS Photonics* **2018**, *5*, 2524.
- [26] Q. Dong, Y. Fang, Y. Shao, P. Mulligan, J. Qiu, L. Cao, J. Huang, *Science* **2015**, *347*, 967.
- [27] Y. Yang, Y. Yan, M. Yang, S. Choi, K. Zhu, J. M. Luther, M. C. Beard, *Nat. Commun.* **2015**, *6*, 7961.
- [28] D. Shi, V. Adinolfi, R. Comin, M. Yuan, E. Alarousu, A. Buin, Y. Chen, S. Hoogland, A. Rothenberger, K. Katsiev, Y. Losovyj, X. Zhang, P. A. Dowben, O. F. Mohammed, E. H. Sargent, O. M. Bakr, *Science* **2015**, *347*, 519.
- [29] Y. Lei, Y. Chen, R. Zhang, Y. Li, Q. Yan, S. Lee, Y. Yu, H. Tsai, W. Choi, K. Wang, Y. Luo, Y. Gu, X. Zheng, C. Wang, C. Wang, H. Hu, Y. Li, B. Qi, M. Lin, Z. Zhang, S. A. Dayeh, M. Pharr, D. P. Fenning, Y.-H. Lo, J. Luo, K. Yang, J. Yoo, W. Nie, S. Xu, *Nature* **2020**, *583*, 790.
- [30] F. Yao, J. Peng, R. Li, W. Li, P. Gui, B. Li, C. Liu, C. Tao, Q. Lin, G. Fang, *Nat. Commun.* **2020**, *11*, 1194.
- [31] Y. He, C. C. Stoumpos, I. Hadar, Z. Luo, K. M. McCall, Z. Liu, D. Y. Chung, B. W. Wessels, M. G. Kanatzidis, *J. Am. Chem. Soc.* **2021**, *143*, 2068.
- [32] Y. Wang, F. Yang, X. Li, F. Ru, P. Liu, L. Wang, W. Ji, J. Xia, X. Meng, *Adv. Funct. Mater.* **2019**, *29*, 1904913.
- [33] Y. Zhong, K. Liao, W. Du, J. Zhu, Q. Shang, F. Zhou, X. Wu, X. Sui, J. Shi, S. Yue, Q. Wang, Y. Zhang, Q. Zhang, X. Hu, X. Liu, *ACS Nano* **2020**, *14*, 15605.
- [34] Z. Gu, Z. Huang, C. Li, M. Li, Y. Song, *Sci. Adv.* **2018**, *4*, eaat2390.
- [35] K. Leng, I. Abdelwahab, I. Verzhbitskiy, M. Telychko, L. Chu, W. Fu, X. Chi, N. Guo, Z. Chen, Z. Chen, C. Zhang, Q.-H. Xu, J. Lu, M. Chhowalla, G. Eda, K. P. Loh, *Nat. Mater.* **2018**, *17*, 908.
- [36] Z. Chen, Q. Dong, Y. Liu, C. Bao, Y. Fang, Y. Lin, S. Tang, Q. Wang, X. Xiao, Y. Bai, Y. Deng, J. Huang, *Nat. Commun.* **2017**, *8*, 1890.
- [37] Y. Wang, X. Sun, Z. Chen, Y.-Y. Sun, S. Zhang, T.-M. Lu, E. Wertz, J. Shi, *Adv. Mater.* **2017**, *29*, 1702643.
- [38] J. Chen, D. J. Morrow, Y. Fu, W. Zheng, Y. Zhao, L. Dang, M. J. Stolt, D. D. Kohler, X. Wang, K. J. Czeck, M. P. Hautzinger, S. Shen, L. Guo, A. Pan, J. C. Wright, S. Jin, *J. Am. Chem. Soc.* **2017**, *139*, 13525.
- [39] J. Jiang, X. Sun, X. Chen, B. Wang, Z. Chen, Y. Hu, Y. Guo, L. Zhang, Y. Ma, L. Gao, F. Zheng, L. Jin, M. Chen, Z. Ma, Y. Zhou, N. P. Padture, K. Beach, H. Terrones, Y. Shi, D. Gall, T.-M. Lu, E. Wertz, J. Feng, J. Shi, *Nat. Commun.* **2019**, *10*, 4145.
- [40] D. Prochowicz, P. Yadav, M. Saliba, D. J. Kubicki, M. M. Tavakoli, S. M. Zakeeruddin, J. Lewiński, L. Emsley, M. Grätzel, *Nano Energy* **2018**, *49*, 523.
- [41] Z. Li, Z. Chen, Y. Yang, Q. Xue, H.-L. Yip, Y. Cao, *Nat. Commun.* **2019**, *10*, 1027.
- [42] D. Li, D. Zhou, W. Xu, X. Chen, G. Pan, X. Zhou, N. Ding, H. Song, *Adv. Funct. Mater.* **2018**, *28*, 1804429.
- [43] G. H. Ahmed, J. K. El-Demellawi, J. Yin, J. Pan, D. B. Velusamy, M. N. Hedhili, E. Alarousu, O. M. Bakr, H. N. Alshareef, O. F. Mohammed, *ACS Energy Lett.* **2018**, *3*, 2301.
- [44] M. Gong, M. Alamri, D. Ewing, S. M. Sadeghi, J. Z. Wu, *Adv. Mater.* **2020**, *32*, 2002163.
- [45] M. I. Saidaminov, M. A. Haque, J. Almutlaq, S. armah, X.-H. Miao, R. Begum, A. A. Zhumekenov, I. Dursun, N. Cho, B. Murali, O. F. Mohammed, T. Wu, O. M. Bakr, *Adv. Opt. Mater.* **2017**, *5*, 1600704.
- [46] D. N. Dirin, I. Cherniukh, S. Yakunin, Y. Shynkarenko, M. V. Kovalenko, *Chem. Mater.* **2016**, *28*, 8470.
- [47] Z. Cheng, K. Liu, J. Yang, X. Chen, X. Xie, B. Li, Z. Zhang, L. Liu, C. Shan, D. Shen, *ACS Appl. Mater. Interfaces* **2019**, *11*, 34144.
- [48] L. Ji, M. D. McDaniel, S. Wang, A. B. Posadas, X. Li, H. Huang, J. C. Lee, A. A. Demkov, A. J. Bard, J. G. Ekerdt, E. T. Yu, *Nat. Nanotechnol.* **2015**, *10*, 84.
- [49] S. Adachi, *Properties of Semiconductor Alloys: Group-IV, III-V and II-VI Semiconductors*, Wiley, NY, USA **2009**.
- [50] D. Lee, H. Lu, Y. Gu, S.-Y. Choi, S.-D. Li, S. Ryu, T. R. Paudel, K. Song, E. Mikheev, S. Lee, S. Stemmer, D. A. Tenne, S. H. Oh, E. Y. Tsybal, X. Wu, L.-Q. Chen, A. Gruverman, C. B. Eom, *Science* **2015**, *349*, 1314.
- [51] Y. El Ajjouri, F. Palazon, M. Sessolo, H. J. Bolink, *Chem. Mater.* **2018**, *30*, 7423.
- [52] L. Ji, Y. Fang, Z. Cheng, Y. Liu, J. Wang, Z. Li, Y. Qian, F. Liu, W. Xu, Z. Wu, F. Wang, A. Wang, L. Wang, Y. Di, W. Huang, T. Qin, *Adv. Mater. Technol.* **2022**, *7*, 2100392.
- [53] Y. Li, Z. Shi, L. Lei, F. Zhang, Z. Ma, D. Wu, T. Xu, Y. Tian, Y. Zhang, G. Du, C. Shan, X. Li, *Chem. Mater.* **2018**, *30*, 6744.
- [54] X. Zhan, X. Zhang, Z. Liu, C. Chen, L. Kong, S. Jiang, S. Xi, G. Liao, X. Liu, *ACS Appl. Mater. Interfaces* **2021**, *13*, 45744.
- [55] Y. Zhai, X. Bai, G. Pan, J. Zhu, H. Shao, B. Dong, L. Xu, H. Song, *Nanoscale* **2019**, *11*, 2484.
- [56] A. Rose, *Phys. Rev.* **1955**, *97*, 1538.
- [57] P. Mark, W. Helfrich, *J. Appl. Phys.* **1962**, *33*, 205.
- [58] Y. Liu, J. Guo, E. Zhu, L. Liao, S.-J. Lee, M. Ding, I. Shakir, V. Gambin, Y. Huang, X. Duan, *Nature* **2018**, *557*, 696.
- [59] R. H. Bube, *J. Appl. Phys.* **1962**, *33*, 1733.
- [60] V. K. Ravi, G. B. Markad, A. Nag, *ACS Energy Lett.* **2016**, *1*, 665.
- [61] P. Gui, H. Zhou, F. Yao, Z. Song, B. Li, G. Fang, *Small* **2019**, *15*, 1902618.
- [62] J. Zhu, M. Tang, B. He, K. Shen, W. Zhang, X. Sun, M. Sun, H. Chen, Y. Duan, Q. Tang, *Chem. Eng. J.* **2021**, *404*, 126548.
- [63] D. Zhang, Y. Yang, Y. Bekenstein, Y. Yu, N. A. Gibson, A. B. Wong, S. W. Eaton, N. Kornienko, Q. Kong, M. Lai, A. P. Alivisatos, S. R. Leone, P. Yang, *J. Am. Chem. Soc.* **2016**, *138*, 7236.
- [64] M. I. Saidaminov, V. Adinolfi, R. Comin, A. L. Abdelhady, W. Peng, I. Dursun, M. Yuan, S. Hoogland, E. H. Sargent, O. M. Bakr, *Nat. Commun.* **2015**, *6*, 8724.

- [65] W.-Q. Liang, Y. Li, J.-L. Ma, Y. Wang, J.-J. Yan, X. Chen, D. Wu, Y.-T. Tian, X.-J. Li, Z.-F. Shi, *Nanoscale* **2020**, *12*, 17213.
- [66] N. Huo, G. Konstantatos, *Nat. Commun.* **2017**, *8*, 572.
- [67] C. Liu, S. Ding, Q. Tian, X. Hong, W. Su, L. Tang, L. Wang, M. Zhang, X. Liu, Y. Lv, J. C. Ho, L. Liao, X. Zou, *Laser Photonics Rev.* **2022**, 2200486.
- [68] F. Wu, Q. Li, P. Wang, H. Xia, Z. Wang, Y. Wang, M. Luo, L. Chen, F. Chen, J. Miao, X. Chen, W. Lu, C. Shan, A. Pan, X. Wu, W. Ren, D. Jariwala, W. Hu, *Nat. Commun.* **2019**, *10*, 4663.
- [69] V. Adinolfi, O. Ouellette, M. I. Saidaminov, G. Walters, A. L. Abdelhady, O. M. Bakr, E. H. Sargent, *Adv. Mater.* **2016**, *28*, 7264.
- [70] D. Kufer, G. Konstantatos, *Nano Lett.* **2015**, *15*, 7307.
- [71] Y. Wang, Z. Wan, Q. Qian, Y. Liu, Z. Kang, Z. Fan, P. Wang, Y. Wang, C. Li, C. Jia, Z. Lin, J. Guo, I. Shakir, M. Goorsky, X. Duan, Y. Zhang, Y. Huang, X. Duan, *Nat. Nanotechnol.* **2020**, *15*, 768.
- [72] X. Wu, S. Hu, H. Shao, L. Li, W. Chen, B. Dong, L. Xu, W. Xu, D. Zhou, Z. Wu, H. Song, X. Bai, *Inorg. Chem. Front.* **2022**, *9*, 44.
- [73] X. Zhang, X. Bai, H. Wu, X. Zhang, C. Sun, Y. Zhang, W. Zhang, W. Zheng, W. W. Yu, A. L. Rogach, *Angew. Chem., Int. Ed.* **2018**, *57*, 3337.
- [74] Y. Fu, H. Zhu, J. Chen, M. P. Hautzinger, X.-Y. Zhu, S. Jin, *Nat. Rev. Mater.* **2019**, *4*, 169.
- [75] X. Zhu, L. Ge, Y. Wang, M. Li, R. Zhang, M. Xu, Z. Zhao, W. Lv, R. Chen, *Adv. Opt. Mater.* **2021**, *9*, 2100058.
- [76] Z.-J. Yong, S.-Q. Guo, J.-P. Ma, J.-Y. Zhang, Z.-Y. Li, Y.-M. Chen, B.-B. Zhang, Y. Zhou, J. Shu, J.-L. Gu, L.-R. Zheng, O. M. Bakr, H.-T. Sun, *J. Am. Chem. Soc.* **2018**, *140*, 9942.
- [77] X. Zheng, Y. Hou, H.-T. Sun, O. F. Mohammed, E. H. Sargent, O. M. Bakr, *J. Phys. Chem. Lett.* **2019**, *10*, 2629.
- [78] D. P. Nenon, K. Pressler, J. Kang, B. A. Koscher, J. H. Olshansky, W. T. Osowiecki, M. A. Koc, L.-W. Wang, A. P. Alivisatos, *J. Am. Chem. Soc.* **2018**, *140*, 17760.
- [79] G. H. Ahmed, J. Yin, R. Bose, L. Sinatra, E. Alarousu, E. Yengel, N. M. AlYami, M. I. Saidaminov, Y. Zhang, M. N. Hedhili, O. M. Bakr, J.-L. Brédas, O. F. Mohammed, *Chem. Mater.* **2017**, *29*, 4393.
- [80] A. Pan, B. He, X. Fan, Z. Liu, J. J. Urban, A. P. Alivisatos, L. He, Y. Liu, *ACS Nano* **2016**, *10*, 7943.
- [81] D. Ren, H. Zhou, R. Chen, D. Wu, H. Pan, J. Zhang, J. Duan, H. Wang, *J. Phys. Chem. Lett.* **2022**, *13*, 267.